Atmospheric Research, 31 (1994) 271–298
Elsevier Science B.V., Amsterdam

Light scattering by nonspherical particles: Remote sensing and climatic implications

K.N. Liou and Y. Takano
Department of Meteorology/CARSS, University of Utah, Salt Lake City, UT 84112, USA

(Received December 8, 1992; revised and accepted April 20, 1993)

ABSTRACT

Calculations of the scattering and absorption properties of ice crystals and aerosols, which are usually nonspherical, require specific methodologies. There is no unique theoretical solution for the scattering by nonspherical particles. Practically, all the numerical solutions for the scattering of nonspherical particles, including the exact wave equation approach, integral equation method, and discrete-dipole approximation, are applicable only to size parameters less than about 20. Thus, these methods are useful for the study of radiation problems involving nonspherical aerosols and small ice crystals in the thermal infrared wavelengths. The geometric optics approximation has been used to evaluate the scattering, absorption and polarization properties of hexagonal ice crystals whose sizes are much larger than the incident wavelength. This approximation is generally valid for hexagonal ice crystals with size parameters larger than about 30.

From existing laboratory data and theoretical results, we illustrate that nonspherical particles absorb less and have a smaller asymmetry factor than the equal-projected area/volume spherical counterparts. In particular, we show that hexagonal ice crystals exhibit numerous halo and arc features that cannot be obtained from spherical particles; and that ice crystals scatter more light in the 60° to 140° scattering angle regions than the spherical counterparts.

Satellite remote sensing of the optical depth and height of cirrus clouds using visible and IR channels must use appropriate phase functions for ice crystals. Use of an equivalent sphere model would lead to a significant overestimation and underestimation of the cirrus optical depth and height, respectively. Interpretation of the measurements for polarization reflected from sunlight involving cirrus clouds cannot be made without an appropriate ice crystal model. Large deviations exist for the polarization patterns between spheres and hexagonal ice crystals. Interpretation of lidar backscattering and depolarization signals must also utilize the scattering characteristics of hexagonal ice crystals.

Equivalent spherical models substantially underestimate the broadband solar albedos of ice crystal clouds because of stronger forward scattering and larger absorption by spherical particles than hexagonal ice crystals. We illustrate that the net cloud radiative forcing at the top of the atmosphere involving most cirrus clouds is positive, implying that the IR greenhouse effect outweighs the solar albedo effect. If the radiative properties of equivalent spheres are used, a significant increase in cloud radiative forcing occurs. Using a one-dimensional cloud and climate model, we further demonstrate that there is sufficient model sensitivity, in terms of temperature increase, to the use of ice crystal models in radiation calculations.

RÉSUMÉ

Les calculs des propriétés de diffusion et d'absorption des cristaux de glace et des aérosols qui en règle générale ne sont pas sphériques requièrent des méthodologies spécifiques. Il n'existe pas de solution théorique unique pour la diffusion par des particules non sphériques. Pratiquement, toutes les solutions numériques pour la diffusion des particules non sphériques, parmi

SSDI 0169-8095(93)E0014-P

lesquelles l'équation d'onde exacte, la méthode par integration et l'approximation à des dipôles discrets, ne sont applicables qu'à des paramètres de dimension inférieurs à 20. Ces méthodes sont donc utiles pour l'étude des problèmes radiatifs relatifs aux aérosols non sphériques et aux petits cristaux de glace dans les longueurs d'onde de l'infrarouge thermique. L'approximation à l'optique géométrique a été employée pour évaluer les propriétés de diffusion, d'absorption et de polarisation des cristaux de glace hexagonaux dont les dimensions sont beaucoup plus élevées que la longueur d'onde incidente. Cette approximation est en général valable pour des cristaux hexagonaux dont les paramètres de dimension sont superieurs à 30.

D'après des données de laboratoire et des résultats théoriques, on montre que les particules non sphériques absorbent moins et ont un plus petit facteur d'asymétrie que les particules sphériques de surface/volume projeté équivalent. On montre en particulier que les cristaux de glace hexagonaux développent de nombreux phénomènes de halo et d'arc qui ne peuvent pas être obtenus à partir de particules sphériques. On montre également que les cristaux diffusent davantage de lumière vers 60° et 140° que les particules sphériques.

Les mesures par satellite de l'épaisseur optique et de l'altitude des cirrus dans les canaux visibles et infrarouges doivent utiliser les fonctions de phase relatives aux cristaux de glace. L'utilisation d'un modèle d'équivalence à une sphère conduirait à une surestimation appréciable de l'épaisseur optique des cirrus et à une sous-estimation de leur atltitude. L'interprétation des mesures de polarisation par les cirrus ne peut pas être faite sans un modèle approprié aux cristaux de glace. On trouve de fortes différences entre les modèles de polarisation par des sphères et des cristaux de glace hexagonaux. L'interprétation des signaux lidar de rétrodiffusion et de dépolarisation doit également utiliser les propriétés diffusantes des cristaux de glace hexagonaux.

Les modèles d'équivalence sphérique sous-estiment fortement les albédos solaires des nuages de glace à cause d'une diffusion avant et d'une absorption plus forte par les particules sphériques que par les cristaux de glace hexagonaux. On montre que le forçage radiatif net à la partie supérieure de l'atmosphère chargée de cirrus est positif, de sorte que l'effet infrarouge de serre dépasse l'effet d'albédo solaire. Si on utilise les propriétés radiatives des sphères équivalentes, on trouve une augmentation significative du forcage radiatif par les nuages. A l'aide d'un modèle de nuage et de climat à une dimension, on démontre en outre que la sensibilité du modèle, en terme d'augmentation de température, permet d'utiliser les modèles relatifs aux cristaux de glace dans les calculs radiatifs.

1. INTRODUCTION

The Earth's atmosphere contains various types of particulates ranging from aerosols, water droplets, and ice crystals, to raindrops and snowflakes. Typical sizes of these particulates are listed in Table 1. Scattering and absorption processes depend both on the incident wavelength and particle size, shape, and orientation. A term referred to as the size parameter, defined as the ratio of the circumference of a particle to the incident wavelength, λ, is commonly used to infer the relative importance of scattering with respect to a specific type of particle. For a spherical particle with a radius a, it is given by $2\pi a/\lambda$. For a nonspherical particle, an appropriate equivalent radius is generally used to define the size parameter.

Also listed in Table 1 are the size parameters using representative wavelengths in the visible, IR and microwave spectra. Aerosols are usually considered to be important in the solar spectrum in view of their size parameters.

TABLE 1

Sizes and size parameters for atmospheric particulates

Type	Size (a)	Size parameters ($2\pi a/\lambda$)		
		λ_v (0.5 μm)	λ_{ir} (10 μm)	λ_m (1 cm)
Aerosol (S*/NS†)	$\lesssim 1$ μm	1.26×10^{1}	6.3×10^{-1}	6.3×10^{-4}
Water Droplet (S)	~ 10 μm	1.26×10^{2}	6.3×10^{0}	6.3×10^{-3}
Ice Crystal (NS)	$\sim 10^2$ μm	1.26×10^{3}	5.3×10^{1}	6.3×10^{-2}
Raindrop (NS)	~ 1 mm	1.26×10^{4}	6.3×10^{2}	6.3×10^{-1}
Snowflakes (Hailstone) (NS)	~ 1 cm	1.26×10^{5}	6.3×10^{3}	6.3×10^{0}

*Spherical; †Nonspherical.

Water droplets and ice crystals are both important in the transfer of solar radiation. Because water clouds are generally opaque in the infrared, the effects of scattering in the thermal IR wavelengths appear to be secondary. Ice clouds, however, are usually semi-transparent and because of the large size parameters for ice particles in the infrared, the scattering processes can play an important role in the transfer of thermal infrared radiation in which the ice's absorption is relatively small.

The shape of aerosols is dependent on their compositions. Solid aerosols are generally irregular. The shape of soluble aerosols (e.g. sulfuric acid) depends on the relative humidity and can be spherical. Because of their sizes, water droplets are usually spherical. Precipitation particles, however, are usually nonspherical. The shape of ice crystals that occur in the atmosphere varies greatly. Laboratory experiments show that the shape and size of an ice crystal is governed by the temperature and supersaturation. In the atmosphere, if the crystal growth involves collision and coalescence, the shapes of ice crystals can be extremely complex. Generally, ice crystals have a basic hexagonal structure. Clearly, a large portion of atmospheric suspensions are nonspherical particles. In view of the size parameters for aerosols and ice crystals and their ubiquitous nature, the scattering processes of these particles play an important role in the radiation budget of the atmosphere as well as in the remote sensing of the atmosphere and the surface.

The Mie theory provides an exact scattering solution for homogeneous isotropic, as well as for concentric nonhomogeneous spheres. However, an exact scattering theory for the solution of nonspherical particles covering all size parameters does not exist in practical terms. Various methodologies and approximations have been developed to solve the scattering and absorption problems involving specific types of nonspherical particles in a limited size parameter region. These methods are reviewed in the second section. In the third section, we present the critical differences in scattering and absorption properties between nonspherical and spherical particles. Implications of these

differences in the interpretation of satellite radiances, polarization measurements from space, and lidar backscattering data are discussed in the fourth section. The fifth section illustrates that the scattering and absorption properties of hexagonal ice crystals are important in the analysis of solar albedo and cloud radiative forcing involving cirrus clouds. Climatic temperature perturbations involving cirrus clouds using hexagonal and spherical models for ice crystals are also performed and assessed using a one-dimensional cloud and climate model. Finally, summary and conclusions are given in the last section.

A REVIEW ON THE METHODOLOGIES USED FOR DETERMINING LIGHT SCATTERING BY NONSPHERICAL PARTICLES

Exact wave equation approach

This approach begins with Maxwell's equations from which the vector equation can be derived. If an appropriate coordinate system can be defined and imposed, we may perform a separation of variables similar to the Mie theory, leading to the solution of the electric and magnetic field vectors of the incident wave in terms of a number of mathematical functions. Subsequently, the scattered electric field at larger distance from the scatterer may be evaluated. Rayleigh (1918) has derived the exact solution for the scattering of a homogeneous dielectric infinite circular cylinder for normal incidence. The case involving arbitrarily oblique incidence has been solved by Wait (1955). Subsequent numerical investigations concerning scattering by infinite circular cylinders have been carried out by van de Hulst (1957), Greenberg et al. (1967), Kerker (1969) and Liou (1972). In particular, Liou (1972) applied the cylindrical solution, for the first time, to model the scattering of light from ice clouds composed of nonspherical ice crystals.

An exact scattering solution for particles with spheroidal shapes has been derived by Asano and Yamamoto (1975). The spheroidal coordinates are obtained by rotating an ellipse about an axis of symmetry and are defined by the angular coordinate, the radial distance, and the azimuthal angle. The parameters can be related to the Cartesian coordinates by an appropriate transformation. If ψ satisfies the scalar wave equation

$$\nabla^2\psi + k^2 m^2 \psi = 0, \tag{1}$$

where k $(=2\pi/\lambda)$ is the wave number, λ is the wavelength and m is the index of refraction, then vectors associated with electric and magnetic fields can be expressed in the spheroidal coordinate system such that they satisfy the vector wave equations, which can be derived by replacing ψ with electric and magnetic vectors. The scalar wave equations can then be expressed in terms of scalar spheroidal wave functions.

The two-by-two amplitude matrix that transforms the incident electric vector into the scattered electric vector in the far field may be written in the form

$$\begin{bmatrix} E_l \\ E_r \end{bmatrix} = \frac{\exp(-ikR+ikz)}{ikR} \begin{bmatrix} S_2 & S_3 \\ S_4 & S_1 \end{bmatrix} \begin{bmatrix} E_l^0 \\ E_r^0 \end{bmatrix}. \tag{2}$$

The term z is the vertical direction in the Cartesian coordinates; R is the distance; $i=\sqrt{-1}$; E_l and E_r represent the electric fields parallel (E_l) and perpendicular (r) to a reference plane, commonly denoted as the plane containing the incident and scattered directions (the scattering plane); and the superscript o denotes the incident field. The amplitude functions for spheroids have been derived by Asano and Yamamoto (1975) and are given by

$$S_i(\theta,\phi) = \sum_{m=0}^{\infty} \sum_{n=m}^{\infty} [\alpha_{i,mn}\sigma_{mn}(\theta) + \beta_{i,mn}\chi_{mn}(\theta)]\cos m\phi, \tag{3a}$$

$$S_{i+2}(\theta,\phi) = \sum_{m=0}^{\infty} \sum_{n=m}^{\infty} [\alpha_{i,mn}\chi_{mn}(\theta) + \beta_{i,mn}\sigma_{mn}(\theta)]\sin m\phi, \qquad i=1,2, \tag{3b}$$

where θ and ϕ are polar and azimuthal angles with respect to the symmetric axis of the spheroid and

$$\sigma_{mn}(\theta) = \frac{mS_{mn}(\cos\theta)}{\sin\theta}, \chi_{mn}(\theta) = \frac{d}{d\theta} S_{mn}(\cos\theta), \tag{4}$$

with S_{mn} being the spheroidal angular function. The terms α_i and β_i are coefficients that can be determined from the four boundary conditions for the electric and magnetic fields at the surface of a spheroid. They are functions of the orientational angles of the spheroid, incident wavelength, refractive index, and aspect ratio. From the amplitude functions, the scattering phase matrix and the scattering and extinction cross sections can be obtained.

Scattering and absorption computations for randomly oriented spheroids have been carried out by Assano and Sato (1980). For the phase function, the rainbow features produced by spheres are absent in the case of spheroids, which also show smaller backscattering. There are also significant differences in the linear polarization patterns and in scattering phase matrix elements. Note that for spheres, there are only four independent elements, whereas six elements are involved for randomly oriented nonspherical particles. It is not computationally feasible to obtain the scattering and polarization properties of nonspherical particles by replacing them with area- (or volume-) equivalent spheres.

Computations of the amplitude functions involve the evaluation of the coefficients α_i and β_i, which are dependent on the size parameter, $2\pi a/\lambda$, where a is the semi-major axis of the spheroid. For size parameters larger than about 20, the spheroidal angular function becomes computationally instable. For

this reason, the method has been applied to size parameters less than about 20. An efficient numerical technique must be developed to extend the method to larger size parameters.

Integral equation method

In this approach, a solution is sought for the scattering field in terms of the incident field and the physical characteristics of the scattering object. Consider a scattering volume bounded by a closed smooth surface, S, and let $\vec{E}^{\mathrm{i}}(\vec{r})$ denote the incident electric field at any point, $\vec{r}$, with respect to an origin inside the scatterer. The scattered electric field may then be determined by

$$\vec{E}^{\mathrm{s}}(\vec{r}) = \vec{\nabla} \times \int_{\mathrm{s}} [\vec{n} \times \vec{E}^{\mathrm{t}}(\vec{r}')] g(k\vec{R}) \mathrm{d}S' -$$

$$\vec{\nabla} \times \vec{\nabla} \times \int_{\mathrm{s}} \frac{1}{i\omega\epsilon_0} [\vec{n} \times \vec{H}^{\mathrm{t}}(\vec{r}')] g(k\vec{R}) \mathrm{d}S', \tag{5}$$

where $\vec{n} \times \vec{E}^{\mathrm{t}}$ and $\vec{n} \times \vec{H}^{\mathrm{t}}$ represent the equivalent magnetic and electric surface current densities, respectively; $\vec{E}^{\mathrm{t}}$ and $\vec{H}^{\mathrm{t}}$ are the total electric and magnetic fields external to the scatterer; n is the unit vector normal to the surface; ϵ_0 is the permittivity; $\vec{R} = |\vec{r} - \vec{r}'|$; ω is the circular frequency ($=kc$); and the free space Green's function is defined by

$$g(k\vec{R}) = e^{ik\vec{R}} / (4\pi\vec{R}). \tag{6}$$

The terms in the integrals of Eq. (5) are expanded in terms of the transverse dyadic Green function, which may be expressed by vector spherical harmonics. The total electric field everywhere inside the scatterer can be set to zero so that $-\vec{E}^{\mathrm{i}}(\vec{r}) = \vec{E}^{\mathrm{s}}(\vec{r})$. Equation (5) can then be used to evaluate the total electric field in terms of the incident electric field by expanding all the fields in terms of vector spherical harmonics and by employing their orthogonality properties. The unknown coefficients in the expansion are determined from the boundary conditions at the surface of the scatterer that require the continuity of the tangential components of the electric and magnetic fields.

The preceding integral equation approach was first developed by Waterman (1965) for perfect conductors. Barber and Yeh (1975) modified this method for the calculation of the scattered electric field for spheroids, which is now known as the Extended Boundary Condition Method (EBCM). Iskander et al. (1983) further improved the EBCM in terms of the stability for the numerical procedure. In a series of papers, Mugnai and Wiscombe (1986, 1989) and Wiscombe and Mugnai (1988) applied the EBCM to irregular shapes with smooth surfaces that can be defined by Chebyshev polynomials. The results show that the scattering and absorption properties for irregularly shaped particles differ significantly from those of the spherical counterparts.

In principle, the EBCM may be used to solve the scattering problem involving any irregular, smooth particle of any size. However, in practice, this method has been used for size parameters less than about 20. For size parameters larger than this limit, numerical instability associated with the expanded spherical harmonics occurs. There are also computational difficulties with this method in the case of highly elongated or flattened particles and a significant computational effort is required for concave particles.

Discrete-dipole approximation

The discrete-dipole approximation is a numerical technique for the calculation of scattering and absorption properties of nonspherical particles. The particle is modeled by an array of N-point dipoles at position $\vec{r}_i$ with polarizabilities $\vec{\alpha}_i$. The total electric field at the position of each dipole, $\vec{E}(\vec{r}_i)$, is the sum of the electric field corresponding to an incident wave and the electric field generated from contributions from all other dipoles as follows:

$$\vec{E}(\vec{r}_i)=\vec{E}_{\text{inc,i}}+\vec{E}_{\text{self},i}, \tag{7}$$

where

$$\vec{E}_{\text{inc},i}=\vec{E}_0 \exp(i\vec{k}\cdot\vec{r}_i-i\omega t), \tag{8}$$

$$\vec{E}_{\text{self},i}=-\sum_{j\neq i}\vec{A}_{ij}\cdot\vec{P}_j \tag{9}$$

$\vec{E}_0$ is the amplitude vector of the incident electric field, k is the wave number of the incidence wave, ω is the circular frequency and t is the time. The polarization $\vec{P}_i=\vec{\alpha}_i\cdot\vec{E}(\vec{r})$ and the matrix $\vec{A}$ is a $3N\times 3N$ symmetric complex matrix that is dependent on the particle shape. Thus, the basic equation for the discrete-dipole approximation can be written in the form

$$(\vec{\alpha}_i)^{-1}\vec{P}_i+\sum_{j\neq 1}\vec{A}_{ij}\cdot\vec{P}_j=\vec{E}_{\text{inc},i}. \tag{10}$$

Equation (10) can then be used to compute $\vec{P}$, which requires an inversion of the matrix $\vec{A}$. To approximate the actual particle, a large number of dipoles ($>10^3$) is required for particles with dimensions comparable to the wavelength. In this case, efficient numerical techniques must be developed to perform calculations.

The discrete-dipole approximation was first developed by Purcell and Pennypacker (1973) for scattering and absorption calculations involving dielectric grains of cubic shape whose sizes are comparable to or smaller than the wavelength of the incident radiation. Improvements on the numerical techniques for the computations of scattering and absorption properties of rectangular particles have been recently developed by a number of researchers, including Singham and Bohren (1987), Draine (1988), Flatau et al. (1990)

and Goodman et al. (1991). The last authors have extended the scattering calculations to a size parameter of 10 for a cubic particle. Except for cubes, rectangles, and disks, scattering and absorption results for other nonspherical particles have not been presented. While this approximation may work well for small size parameters, innovative numerical approaches are required to apply this method to nonspherical particles with size parameters larger than about 10.

Geometric optics approach

If a particle is much larger than the incident wavelength, the laws of geometric optics may be applied to the scattering of light. In this case, a light beam may be thought of as consisting of a bundle of separate rays that hits the particle. The width of the light beam is much larger than the wavelength and yet small compared with the particle's size. Each ray that hits the particle will undergo reflection and refraction and will pursue its own specific path along a straight line. The rays that emerge from various directions will have different amplitudes and phases. The geometric ray optics approach has been used to identify the positions of various optical phenomena produced by water droplets and ice crystals, such as rainbows and halos (see, e.g., Greenler, 1980; Liou, 1980).

In the geometric optics method, the angles corresponding to incident and refracted rays on a surface are defined by Snell's law: $\sin \theta_i / \sin \theta_t = m$, where m is the index of refraction for the second medium with respect to the first and θ_i and θ_t denote the incident and refracted angles, respectively, with respect to the normal to the surface, for a given ray. The energies that are reflected and refracted from the surface are governed by Fresnel formulas, which are results of continuity requirements for the tangential components of the electric and magnetic vectors at the interface.

Because of the lack of a proper definition of the coordinate system for hexagonal structure, which is typical for ice crystals occurring in the atmosphere, the solution for the scattered electric field by means of the wave equation approach has not been available up to this point. The geometric optics approach has been used to derive the scattering, absorption and polarization properties of hexagonal ice crystals. Consider a hexagonal ice crystal that is arbitrarily oriented with respect to an incident light beam characterized by a specific electric vector. There are eight faces into which light rays may enter. The two components of the electric vectors parallel and perpendicular to the scattering plan can be used in tracing the light rays that undergo reflection and refraction. Electric fields reflected and refracted on a given surface can be computed from Fresnel formulas. The distances between the points of entry and departure, as well as the phase shifts of the electric field due to reflection and refraction, can be evaluated. The electric field vector associated with

all incident rays that undergo external reflection, two refractions, and internal reflections may be obtained by summing the outgoing electric field vectors that have the same direction in space.

Computation of the angular scattering patterns for hexagonal crystals based on the geometric ray-tracing method were first reported by Jacobowitz (1971), assuming infinite long hexagonal columns. A more comprehensive ray-tracing analysis to compute the phase functions for finite hexagonal columns and plates has been undertaken by Wendling et al. (1979) and Coleman and Liou (1981). Cai and Liou (1982) developed a ray-tracing model for arbitrarily oriented hexagonal ice crystals, which takes into account internal absorption and polarization, in which the four-by-four scattering phase matrix can be evaluated. For the first time, diffraction from a hexagonal aperture was also included in the geometric optics method. Along the same line, Takano and Jayaweera (1985), Muinonen et al. (1989), and Rockwitz (1989) also carried out numerical computations for the scattering of oriented hexagonal ice crystals. Takano and Liou (1989) have developed a new geometric ray-tracing program that accounts for the ice crystal size distribution and the possibility of horizontal orientation. Incorporation of the birefringent properties of ice and of the δ-transmission in the 0° scattering angle produced by transmissions through two parallel surfaces are new features that were included in the geometric ray-tracing program. Hexagonal ice crystals have flat surfaces which differ from surfaces involving spheres, circular cylinders and spheroids. Based on the calculations of Takano and Liou (1989) and Takano et al. (1992), it is estimated that the geometric optics approximation is generally valid for hexagonal ice crystals with size parameters larger than about 30.

CRITICAL DIFFERENCES BETWEEN SCATTERING AND ABSORPTION PROPERTIES OF NONSPHERICAL AND SPHERICAL PARTICLES

We shall investigate the differences between the scattering and absorption properties of nonspherical and spherical particles based on results from laboratory measurements as well as theoretical calculations. First, consider the aerosols. Aerosols are important for their influence on solar radiation. The scattering characteristics of aerosols can be measured in the laboratory using the direct method involving ensembles of particles at solar (in particular, visible) wavelengths or the analog experiments that perform similar investigations on individual particles at microwave wavelengths. Interactions of a particle with electromagnetic radiation depend explicitly on the particle size parameter. For this reason, interactions of a particle at solar (visible) wavelengths can be simulated by those in the microwave domain with an appropriately scaled particle. In the analog experiment, the refractive indices of the experimental material at microwave wavelengths must match those of the solar counterpart. Because the analog experiments involve physically large par-

ticles, they can be performed in a much more controlled environment such that shapes, sizes and orientations can be specified in the experiment.

Holland and Gagne (1970) carried out an experiment to measure the scattering phase function for flat plates at a visible wavelength. They found that particles of irregular shape scatter considerably more energy into the side-scatter region than equivalent assemblies of spheres. Using the analogy experiment, Zerull and Giese (1974) and Zerull (1976) and Zerull et al. (1977) measured the scattering patterns for cubes, convex and concave particles with size parameters less than about 20. Recently, Hage et al. (1991) compared theoretical calculations and experiments from a microwave analog experiment including a porous cube.

Figure 1 shows the measured phase function for scattering by an ensemble of randomly oriented convex and concave particles with size parameters between 5.9 and 17.8 and a refractive index of $1.5+0.005i$ determined from the analog experiment (Zerull, 1976). Also shown are the phase functions predicted by the Mie theory for equal volume and equal area spheres and that derived by the semi-empirical theory developed by Pollack and Cuzzi (1980). The scattering pattern for nonspherical particles deviate significantly from that for equivalent spheres. Nonspherical particles scatter much more light in the directions between the 60° and 140° scattering angles.

Measurements of scattering and polarization patterns for ice crystals have been carried out in cold chambers where various shapes and sizes may be generated (Dugin and Mirumyants, 1976; Nikiforova et al., 1977; Sassen and

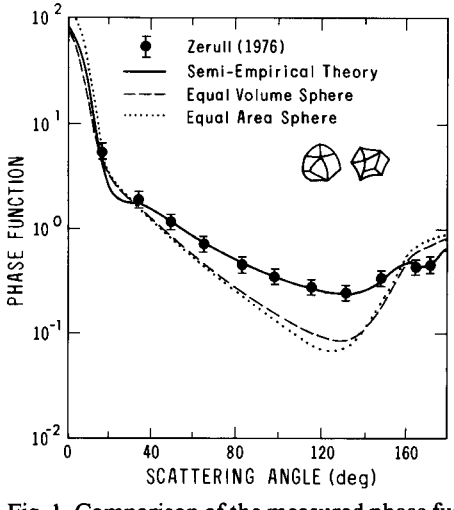

Fig. 1. Comparison of the measured phase function for scattering by an ensemble of convex and concave particles with size parameters ranging from 5.9 to 17.8 determined from a microwave analog experiment (Zerull, 1976) with the results from Mie theory for equal volume and equal area spheres and the semi-empirical theory developed by Pollack and Cuzzi (1980).

Liou, 1979; Volkovitsky et al., 1980). Dugin and Mirumyants measured the scattering phase matrix elements for laboratory clouds containing 20–100 μm plates at the 0.57 μm wavelength. The ice crystals generated in the cold chamber were smaller than those occurring in cirrus clouds. Takano and Liou (1989) compared the theoretical polarization results computed from a geometric ray-tracing program with experimental data. The theoretical results for columns and plates can be used to interpret the measured data.

Figure 2 shows the scattering phase function measured at a wavelength of 0.6328 μm for laboratory clouds containing columns (Volkovitsky et al., 1980). The distinctive features of 22° and 46° halos are produced in the laboratory data. Theoretical ray-tracing results using the ice crystal size distribution for cirrostratus and results from Mie calculations for ice spheres are also shown for comparison. There are general agreements between laboratory scattering data and theoretical ray-tracing results. It is not possible to carry out a precise comparison because the exact sizes for columns were not available, and because the laboratory data lacked values within 10° of forward and backscattering directions due to the limitations of nephelometer measurements. The maximum at about 140° scattering angle for ice spheres is the rainbow feature produced by spherical particles. In comparisons between the phase function patterns for hexagonal columns and ice spheres, significant

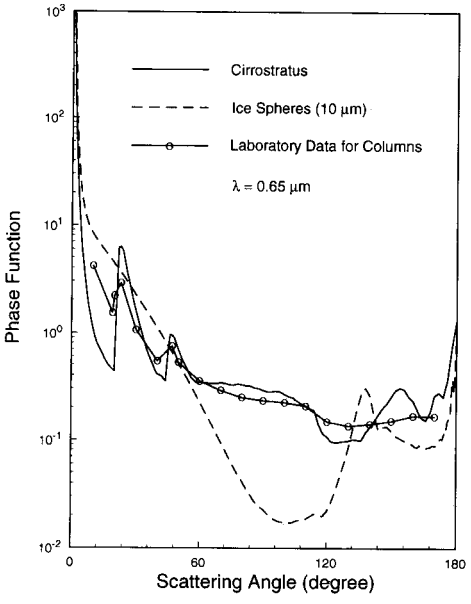

Fig. 2. Comparison of the measured phase function for scattering by columns generated in the cold chamber using the 0.6328 μm wavelength (Volkovitsky et al., 1980) with the theoretical results for randomly oriented ice columns and ice spheres.

differences are present. Hexagonal ice crystals scatter much more light in the side scattering directions from about 60 to 160° scattering angles, except in the vicinity of the rainbow angle. Compared to spheres, hexagonal ice crystals also scatter less in the forward directions.

Finally, we investigate the differences between the single-scattering albedo and asymmetry factor for various sizes of hexagonal ice crystals and area equivalent ice spheres using 0.55 and 2.2 μm (Table 2). Absorption is practically negligible at 0.55 μm. Area equivalent spheres would give approximately the same extinction cross section. For both wavelengths, hexagonal ice crystals have a smaller asymmetry factor than the spherical counterparts. At the 2.2 μm wavelength, hexagonal ice crystals absorb less than the spherical particles. Consider volume equivalent spheres, which would give approximately the same absorption cross section, σ_a, as compared with nonspherical particles. Because of smaller cross sections, volume equivalent spheres would have a smaller scattering cross section, σ_s, resulting in a larger co-single-scattering albedo, $(1-\tilde{\omega})=\sigma_a/(\sigma_a+\sigma_s)$. This implies that volume equivalent spheres would absorb more than nonspherical particles in the context of radiative transfer calculations in which one of the fundamental parameters is the single-scattering albedo.

In summary, we conclude that nonspherical particles absorb less and have a smaller asymmetry factor than their equal-area or equal-volume spherical counterparts. These important features are characteristic not only for ice crystals, but also for nonspherical aerosols. The influence of the shape of tropospheric aerosols on the solar albedo has been investigated by Pollack and Cuzzi (1980) who show that sizable differences in global albedo occur between cases involving nonspherical aerosols and their equivalent spherical counterparts. Little research has been carried out regarding the influence of aerosol shape on the active and passive remote sensing of aerosol concentra-

TABLE 2

Single-scattering albedo, $\tilde{\omega}$, and asymmetry factor, g, for hexagonal ice crystal and area* equivalent ice spheres at $\lambda=0.55$ and 2.2 μm

L/2a (μm/μm)	λ (μm)	1-$\tilde{\omega}$		g	
		Hexagon	Sphere	Hexagon	Sphere
20/20	0.55	0	0	0.7704	0.8759
	2.2	4.085×10^{-2}	4.944×10^{-2}	0.8185	0.8729
120/60	0.55	0	0	0.8155	0.8871
	2.2	1.246×10^{-1}	1.539×10^{-1}	0.8829	0.9174
750/160	0.55	0	0	0.8592	0.8908
	2.2	2.503×10^{-1}	3.583×10^{-1}	0.9380	0.9566

*Give approximately the same extinction cross section.

tions and particle sizes. In the following, we shall confine our discussion to the implications of the nonsphericity of ice crystals on remote sensing and climate modeling.

REMOTE SENSING IMPLICATIONS

A number of examples are given to illustrate the importance of the scattering and absorption properties of ice crystals in the interpretation of satellite radiance observation, polarization measurements from space and lidar backscattering data.

Satellite remote sensing

Visible and IR two-channel technique

Minnis et al. (1992) developed a retrieval algorithm for the inference of the optical depth and height of cirrus clouds using the two-channel technique. The retrieval algorithm includes the following. First, the observed visible reflectance is interpreted with a parameterization of radiative transfer calculations using the scattering characteristics of two specific cloud particle size distributions; a water droplet distribution having an effective radius of 10 μm and an effective variance of 0.05 and an ice crystal size distribution for cirrostratus. The water droplet model distribution, a model used by the ISCCP, was used to compute the Mie-scattering phase function. The phase function for the cirrostratus model was computed from a geometric ray-tracing program developed by Takano and Liou (1989). An optical depth is determined with the radiative transfer parameterization from a given reflectance observation using one of the two models. This parameterization accounts for the surface reflection, Rayleigh scattering and ozone absorption. The visible optical depth is then used to compute the IR emissivity of cirrus clouds, based on a parameterization involving the two. The IR emissivity is subsequently used along with the observed IR radiance to obtain a better estimate of the true radiating temperature of the cloud. This temperature is then converted to cloud height using the nearest available sounding.

Figure 3 shows the effects of nonsphericity on the retrieval of cloud height using GOES visible (0.65 μm) and IR (11.2 μm) data during the FIRE II experiments in southeastern Kansas between November 13 and December 7, 1992 (Minnis et al., 1992). For comparison purposes, the cloud-center heights determined from the NASA Langley lidar are displayed. As shown in this figure, the hexagonal ice crystal model produces cloud center heights which are within 0.2 km of the lidar derived values. The ice sphere model yields underestimates of the cloud heights.

The preceding example illustrates the importance of using the phase function of hexagonal ice crystals in the interpretation of satellite reflectance mea-

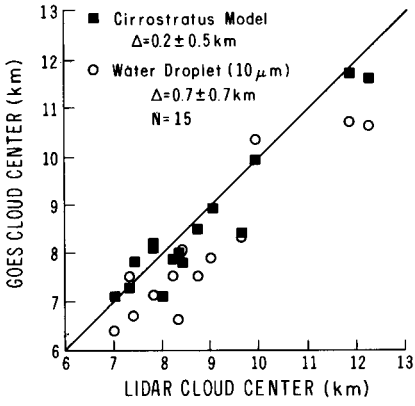

Fig. 3. Comparison of the cloud center height derived from GOES satellite visible and IR radiance measurements and from surface lidar (Minnis et al., 1992, see text for further explanation).

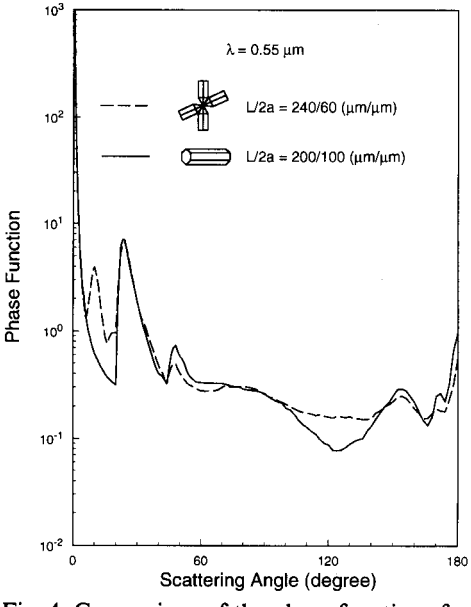

Fig. 4. Comparison of the phase functions for randomly oriented columns and bullet rosettes with the same cross section area.

surements. We notice from Fig. 2 that significant differences in phase functions for ice spheres and hexagonal columns are evident in the region from 60 to 150° scattering angles. Based on cloud physics observations (Heymsfield and Knollenberg, 1972), a substantial portion of ice crystals are bullet rosettes. We have carried out a geometric ray-tracing program using a Monte Carlo method to compute the phase function for randomly oriented bullet

rosettes. Figure 4 shows a comparison of the phase functions for columns and bullet rosettes whose averaged projected areas are the same. In the case of bullet rosettes, an additional maximum is shown at about the 10° scattering angle that is produced by two refractions involving prism and pyramidal planes. In addition, bullet rosettes scatter more light in the scattering angle region from about 100° to 140°. The phase function for bullet rosettes may be of use in the interpretation of bidirectional reflectance.

Ice crystals in thin cirrus clouds could be horizontally oriented. The fact that numerous arcs and halos are visible demonstrates that horizontal orientation must exist for some cirrus clouds. Figure 5 shows the bidirectional reflectances for randomly oriented (3-D) and horizontally oriented (2-D) columns using the cirrostratus size distribution in the plane defined by the emergent (θ) and relative azimuthal ($\phi-\phi_0$) angles. Two optical depths, τ, of 1 and 4 are used and the cosine of the solar zenith angle is 0.5. In the 3-D case, the maximum at $\theta=60°$ in the plane of $\phi-\phi_0=180°$ is associated with the glory-like feature in the 180° backscattering direction. Large values are also shown around the limb direction ($\theta>70°$ in the planes of $0°\leq\phi-\phi_0\leq45°$). Minimum values occur in the vicinity of the zenith direction ($\theta=0°$) for both $\tau=1$ and 4. For $\tau=4$ the reflectance pattern is more isotropic than that for $\tau=1$. A maximum occurs in the 2-D case at about $\theta=60°$ in the plane of $\phi-\phi_0=180°$, corresponding to the sub-anthelion feature produced by one internal reflection (the scattering angle is about 180°). Also, a maximum is located at about $\theta=60°$ in the plane of $\phi-\phi_0=0°$, resulting from the subsun features produced by external reflections (the scattering angle is about 60°). This feature does not exist in the 3-D case. The bidirectional reflectances for 2-D columns are more anisotropic than those for 3-D columns with larger values in the vicinity of subanthelion and subsun positions and smaller values in other directions.

IR brightness temperature difference

Figure 6 shows a scatter diagram of the brightness temperature difference between several IR wavelengths, consisting of several hundred points collected for about four hours under cirrus cloud conditions obtained by the HIS instrument aboard the NASA ER-2 during FIRE I (Ackerman et al., 1990). The envelopes are results determined from a theoretical radiative transfer program corresponding to a large set of data points computed by varying the cloud thickness, size distribution and surface temperature (Takano et al., 1992). The solid curve corresponds to the theoretical results for a nonspherical model involving spheroid/hexagonal particles. If the size parameters are greater than 30, the scattering and absorption properties for hexagonal ice crystals are used. If the size parameters are less than 30, those for spheroids with axial ratios of 3 and 5 are employed. The dashed curve corresponds to results involving area-equivalent spheres. The solid envelope covers the ob-

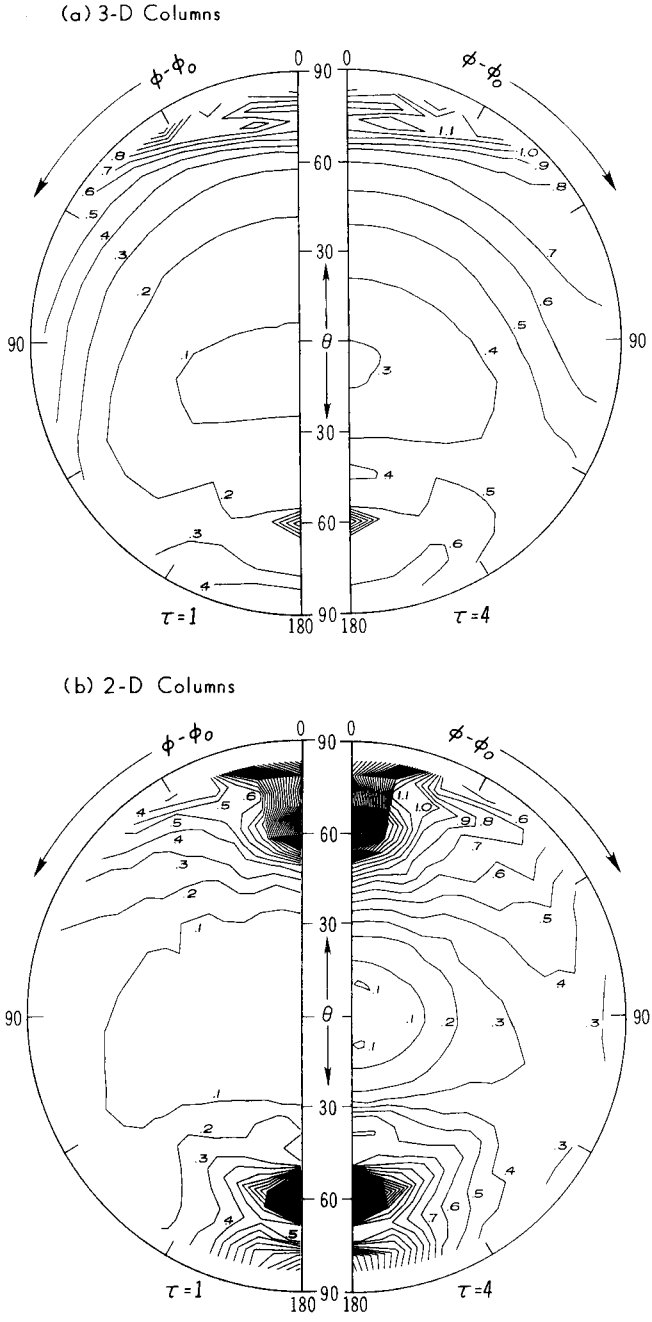

Fig. 5. Bidirectional reflectances for randomly oriented (3-D) and horizontally oriented (2-D) columns in the plane defined by the emergent zenith angle (θ) and relative azimuthal angle ($\phi - \phi_0$) between the position of the sun and satellite. The cosine of the solar zenith angle used in the calculations is 0.5. Results for two optical depths are shown.

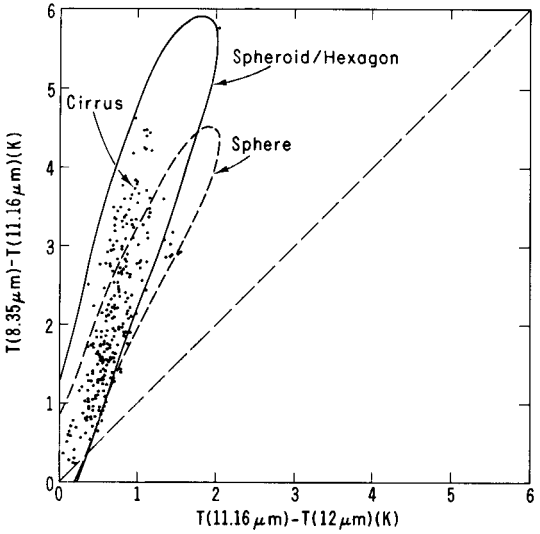

Fig. 6. A scatter diagram of the brightness temperature differences between 11.16 and 12 μm and between 8.35 and 11.16 μm collected by the HIS instrument aboard the NASA ER-2 during FIRE I cirrus IFO (Ackerman et al., 1990). The envelopes are theoretical results computed from a radiative transfer program using an ice crystal model and an ice sphere model. These envelopes correspond to a large set of data points by varying the cloud thickness, size distribution and surface temperature (Takano et al., 1992).

served data for cirrus, whereas the dashed envelope corresponding to equivalent spheres significantly deviates from the observed data. The differences in the single-scattering properties between the 11.16 and 12 μm wavelengths do not significantly depend on the particle shape due to the large absorption property of ice. However, at the 8.35 μm wavelength, equivalent spheres have a smaller single-scattering albedo and, hence, absorb more radiation. Consequently, the brightness temperature for this wavelength is less than that for nonspherical results. The preceding demonstration shows that a better interpretation for the brightness temperature of cirrus clouds can be made by using appropriate nonspherical models.

Polarization and backscattering depolarization measurements

Polarization

Polarization of the reflected sunlight from clouds and aerosols contains information of particle characteristics. In the following, a specific example is given to demonstrate the importance of using a nonspherical particle model to interpret the polarization measurements. Figure 7 shows the linear polarization pattern on the solar principal plane as a function of phase angle (180° -scattering angle) measured from a cirrus cloud with a thickness of 5 km using

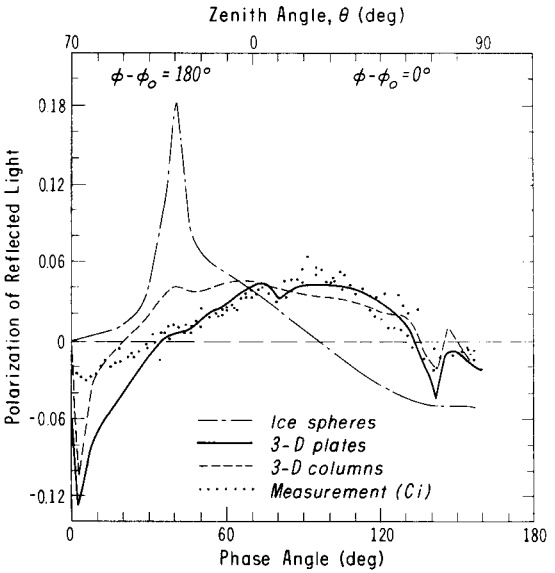

Fig. 7. Linear polarization as a function of phase angle (180° - scattering angle) measured from a cirrus cloud with a thickness of 5 km using the 2.2 μm wavelength (Coffeen, 1979). A number of theoretical results are displayed in the diagram for comparisons, including randomly oriented columns and plates and area equivalent spheres.

a wavelength of 2.22 μm (Coffeen, 1979). Polarization values are generally less than 6% and are positive from 30 to 130° phase angles. A number of theoretical results are also displayed for comparison, including randomly oriented columns and plates and area equivalent spheres.

The computed polarization pattern used an optical depth of 64 and a solar zenith angle of 70° in order to match the observations (Takano and Liou, 1989). For plates and columns, the negative values around the 140° and 160° phase angles result from the 46° and 22° halos, respectively. Results from the spherical model deviate significantly from the observations. Spheres produce maximum polarization at the rainbow angle. This feature does not exist in the observed pattern. The computed polarization for ice plates fits the observed values quite well. It appears that the cloud particles near the cloud top must be randomly oriented plate-like crystals. There are deviations between the computed and observed polarization around the 0° phase angle (backscattering) because scattered light is partially blocked by the aircraft and because the cloud may contain irregular ice crystals, which would reduce polarization in the backscattering directions. Finally, it should be noted that the observed polarization patterns can be used to differentiate between ice and water clouds.

Lidar backscattering depolarization measurements

The depolarization technique has been developed from lidar backscattering returns for the purpose of differentiating between ice and water clouds in the past 20 years. The technique is based on the fundamental scattering properties of ice crystals and water droplets. For spherical water droplets, the incident polarized light beam will retain the polarization state at the backscattering direction if multiple scattering can be neglected. The cross polarized component, called depolarization, of the incident polarized light occurs for nonspherical particles. For ice crystals in the geometric optics region, depolarization is produced by internal reflections and refractions (Liou and Lahore, 1974). A parameter referred to as the depolarization ratio, defined as the ratio of the cross polarized returned power to the return power of the original polarization state, has been used to differentiate between ice and water clouds as well as the physical characteristics of ice crystal clouds.

Figure 8 shows the linear depolarization ratio for various types of ice crystals and water droplets derived from laboratory and field studies (Sassen, 1976). For water droplets, this ratio is close to zero as is predicted from the theory. For pure ice crystals, the depolarization ratio is on the order of 50 to 70%. Large plate and column crystals tend to orient in the direction parallel to the ground. In the case of horizontally oriented plate crystals, the depolarization ratio would be zero because of the symmetry of the two parallel crystal surfaces. Figure 9 illustrates the backscattering coefficient and depolarization ratio as functions of altitude and scan angle (Platt et al., 1978). At the backscattering direction (zenith angle of 0.0°), the depolarization ratio is close to zero. This ratio increases significantly as the lidar scans a few degrees off the

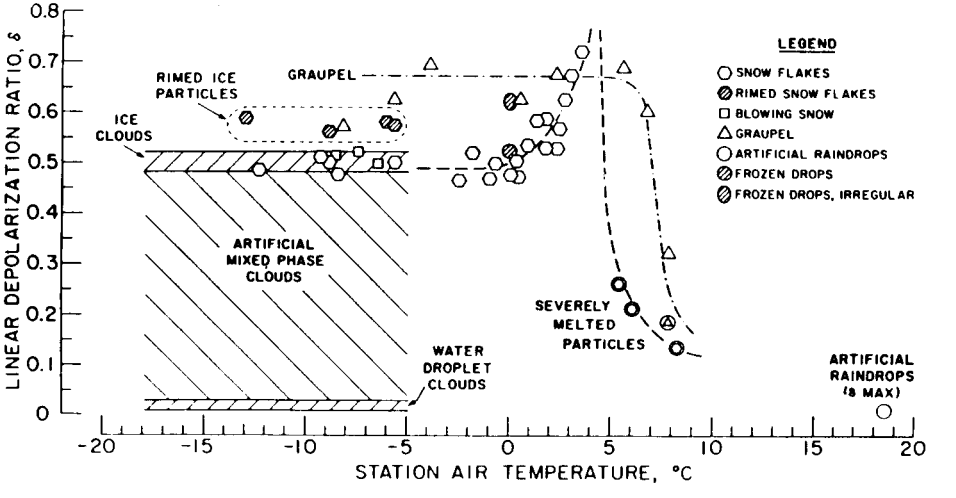

Fig. 8. Depolarization ratio for various types of ice crystals and water droplets derived from laboratory and field studies using the CW laser and lidar approach (Sassen, 1976).

vertical, revealing that the ice clouds, occurring in the temperature range of -9 to $-13.4°C$, must contain horizontally oriented plate crystals. The two preceding examples demonstrate the importance of the scattering characteristics of ice crystals in terms of shape and orientation in the interpretation of the lidar backscattering returns.

The scattering properties of hexagonal columns and plates have been comprehensively computed by Takano and Liou (1989) based on the principle of geometric ray tracing. An example of the scattering phase function for randomly oriented bullet rosettes has also been shown in Fig. 4. The shape of ice crystals is primarily controlled by temperature and supersaturation. Hollow columns occur when excess vapor density over ice is greater than about 0.04 g/m^3 but less than 0.1 g/m^3 (Fletcher, 1962). Figure 10 shows the phase functions for randomly oriented hollow and solid columns with a length of 200 μm and a width of 80 μm for the 0.55 μm wavelength. The depth of the hollow structure is 50 μm on both ends. Significant differences are evident in the backward (140°–180°) and forward (10°–20°) directions. Also, the 46° halo disappears in the case of hollow columns because of the lack of two refractions through the 90° angle. The backscattering for the present hollow

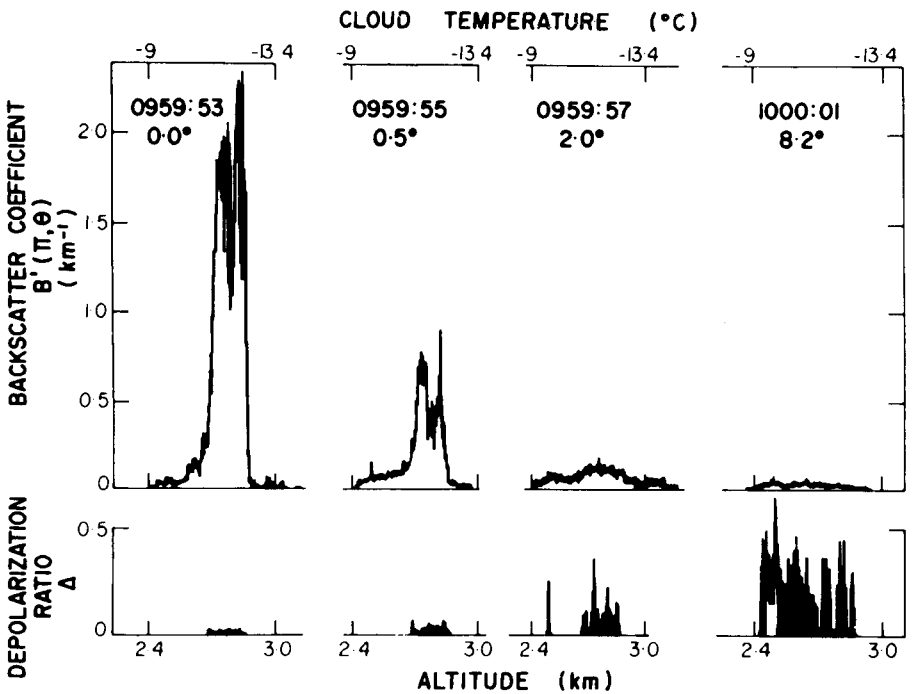

Fig. 9. Cloud backscattering coefficients and depolarization ratios derived from a lidar experiment for a number of vertical scans (Platt et al., 1978).

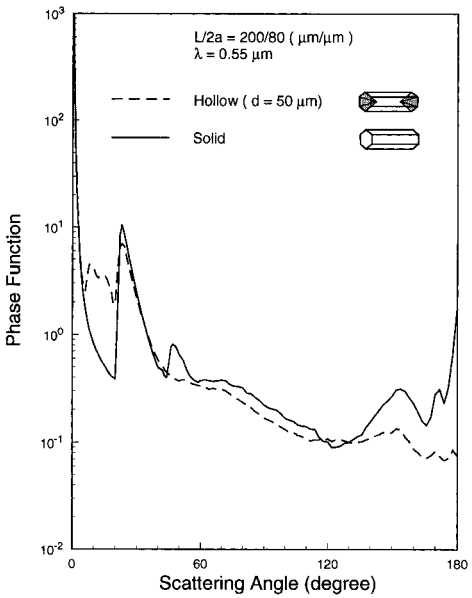

Fig. 10. The phase functions for randomly oriented hollow and solid columns with a length of 200 μm and a width of 80 μm for the 0.55 μm wavelength. The depth of the hollow structure used in the geometric ray-tracing calculation is 50 μm on both ends.

columns is a factor of 20 smaller than that for solid columns. This large difference undoubtably would have a significant effect in the interpretation of lidar backscattering returns in cases when clouds contain hollow ice crystals.

As discussed previously, the shapes of ice crystals that occur in cirrus clouds are dependent on temperature and supersaturation. Interpretation of active and passive remote sensing measurements for the inference of the composition and thickness of cirrus clouds must utilize the scattering and absorption properties of appropriate ice crystal models. Concurrent cloud microphysics observations would assist in the development of remote sensing techniques.

CLIMATIC IMPACT OF CIRRUS CLOUDS

We have pointed out in the discussion of the retrieval of cloud optical depth and cloud height using visible and IR radiances that the bidirectional reflectance from clouds consisting of nonspherical ice crystals is much brighter than the spherical counterparts. The reason is that spherical particles have a larger asymmetry factor and, hence, more light is scattered in the forward directions resulting in weaker backscattering. It is expected that for a given optical depth, clouds composed of nonspherical particles would have larger solar albedos, i.e., larger reflected flux at the cloud top, than spherical particles.

Broadband flux observations from aircraft involving cirrus clouds have been carried out during the FIRE experiment in Wisconsin, October–November, 1986. Results for solar albedo were analyzed by Stackhouse and Stephens (1991) for the October 28 case (Fig. 11). The extensions of the vertical and horizontal lines through the data points denote the uncertainties of measurements. The dashed lines show the theoretical results as functions of the ice water path (IWP) using the observed size distributions converted into equivalent spheres. These results are much smaller than the observed values. The solid lines represent theoretical results using the scattering and absorption properties of hexagonal ice crystals in a radiative transfer parameterization program involving the δ-four-stream method for radiative transfer and the correlated k-distribution for gaseous absorption. The solar albedo values are functions of both IWP (g/m^2) and the mean effective size, defined as the ice crystal width weighted by the cross sectional area of ice particles as follows:

$$D_e = \int_{L_{min}}^{L_{max}} D^2 L n(L) dL \Big/ \int_{L_{min}}^{L_{max}} DL n(L) dL, \tag{11}$$

where D is the width; L the length of an ice crystal; $n(L)$ denotes the ice crystal size distribution; and L_{min} and L_{max} are the minimum and maximum lengths of ice crystals, respectively. The mean size of ice crystals determined from theoretical computations ranges from 50 to 75 μm, in agreement with the observed ice crystal size. It is clear that the spherical assumption is unable to reliably interpret the observed solar albedo values involving cirrus clouds.

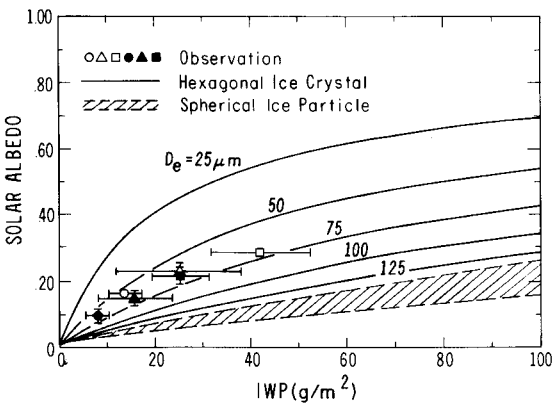

Fig. 11. Solar albedo as a function of ice water path (IWP) determined from broadband flux observations from aircraft involving cirrus clouds during FIRE I cirrus IFO (Stackhouse and Stephens, 1991). The extensions of the vertical and horizontal lines through the data points denote the uncertainties of measurements. The dashed lines show the theoretical results using the observed size distribution converted into equivalent spheres. The solid lines represent theoretical results using the scattering and absorption properties of hexagonal ice crystals in terms of mean effective size, D_e (see text for further explanation).

To quantify the effects of nonspherical particles on the radiation budget of the earth and the atmosphere, we use the cloud radiative forcing concept for the flux at the top of the atmosphere. This forcing is defined as the difference of the clear sky and overcast net fluxes in the form

$$C = C_{\mathrm{ir}} + C_s, \tag{12}$$

where

$$C_{\mathrm{ir,s}} = F^{\mathrm{cl}}_{\mathrm{ir,s}} - F^{\mathrm{ov}}_{\mathrm{ir,s}}, \tag{13}$$

and F^{cl} and F^{ov} denote the flux at the top of the atmosphere for clear and overcast conditions, respectively; the subscript ir denotes the broadband IR, and s the broadband solar components. If C is positive, the IR greenhouse effect outweighs the solar albedo effect and there will be a net gain of energy within the atmosphere. However, if C is negative, the reverse is true. In the calculations, a mean effective size of about 42 μm corresponding to the ice crystal size distribution for Cs was used, along with a cloud base of 9 km, a cosine of the solar zenith angle of 0.5, a solar duration of 12 hours, and a surface albedo of 0.1. The cloud cover employed in this illustration is 100%. Figure 12 shows the cloud radiative forcing, which is expressed in terms of IWP as well as optical depth. In this figure and in Fig. 13, IWP is the independent variable, while the optical depth is calculated by using the extinction coefficient for hexagonal ice crystals. We use the same optical depth for equivalent ice spheres to investigate the effects of the single-scattering albedo and phase function on the cloud radiative forcing and climatic temperature per-

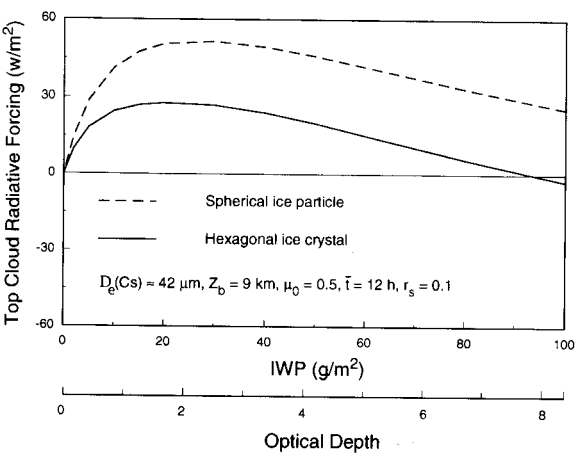

Fig. 12. Cloud radiative forcing at the top of the atmosphere expressed in terms of ice water path (IWP) as well as optical depth. The cloud cover used in the calculation is 100% and other relevant parameters are displayed in the figure. Solid and dashed curves are results using hexagonal ice crystal and ice sphere models.

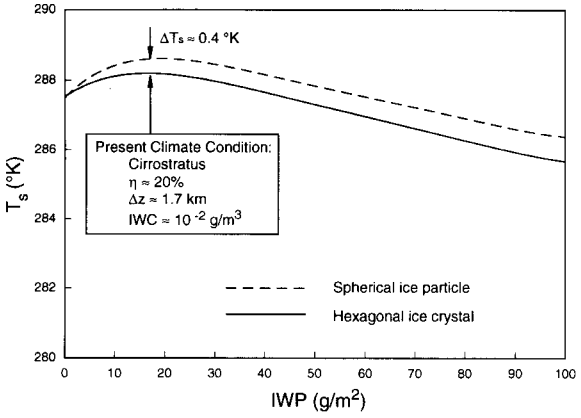

Fig. 13. Surface temperatures determined from a one-dimensional cloud and climate model developed by Liou and Ou (1989). The condition for the present climate is depicted in the diagram. Solid and dashed curves are for results using hexagonal ice crystal and ice sphere models. Feedbacks between temperature and ice water path and ice crystal size are not accounted for in the present model calculations.

turbation. Results involving hexagonal ice crystals show positive radiative forcing, revealing that the greenhouse effect outweighs the solar albedo effect for a realistic range of optical depths for cirrus clouds. This positive forcing is in part produced by the position of cirrus clouds and their downward emission. Using the spherical particle assumption, the cloud radiative forcing values increase substantially. This large increase is a result of the smaller solar albedo values in the case of spherical particles, as shown in Fig. 11. For partly cloudy conditions, cloud radiative forcing can be obtained by multiplying the present results by the fraction of cloud cover.

Finally, we investigate the potential effect of particle nonsphericity in light scattering on the climatic temperature perturbation. Using a onedimensional cloud-climate model developed by Liou and Ou (1989), perturbation calculations were performed by varying the IWP using a Cs cloud model. Cloud positions and covers for high, middle and low cloud types are prescribed. In the perturbation runs, only the IWP of high clouds is varied; all other components remain unchanged. The model simulations use the radiative properties of cirrus clouds involving hexagonal ice crystals and area-equivalent spherical ice particles that are computed from a radiative transfer parameterization program in terms of IWP and Cs size distribution. In the model, the present climate condition, with a surface temperature of 288 K, corresponds to an IWP of about 20 g/m^2, and a cirrus cloud cover of about 20%. Perturbations were carried out by varying the IWP. Figure 13 shows that the surface temperature decreases as the IWP increases. The reason is that the increase in IR emissivity is very small and a significant increase in solar albedo occurs,

resulting in the domination of the solar albedo effect. Using the spherical model, we showed that the cloud radiative forcing increases by about a factor of two because of the reduction of solar albedo. For this reason, larger surface temperatures are produced relative to the case involving the hexagonal ice crystal model. At the present climate condition, the increase amounts to about 0.4 K, which is substantial. In these perturbation exercises, the feedbacks between temperature and particle size and IWP have not been considered. The prime objective of this illustration is to show that using the radiative properties of cirrus clouds for spherical and nonspherical models, sufficient sensitivity in climatic temperature perturbations can be produced.

SUMMARY AND CONCLUSIONS

A large portion of atmospheric suspensions, in particular, aerosols and ice crystals, are nonspherical particles. We have reviewed a number of methodologies for the calculation of the scattering and absorption properties of nonspherical particles with various shapes. Practically, all of the numerical solutions for the scattering of nonspherical particles, including the exact wave equation solution, integral equation method, and discrete-dipole approximation are applicable to size parameters less than about 20. Thus, these methods are useful for the study of radiation problems involving nonspherical aerosols. For hexagonal ice crystals whose sizes are much larger than the incident wavelength, the geometric optics approximation has been used to evaluate the scattering, absorption and polarization properties of these types of particles. This approximation is valid for ice crystal size parameters larger than about 30. From existing laboratory data and theoretical results, we illustrate that nonspherical particles absorb less and have a smaller asymmetry factor than the equal-area or equal-volume spherical counterparts. In particular, we show that hexagonal ice crystals scatter more light in the region from the 60° to 140° scattering angles than the spherical counterparts. It is apparent that exact and approximate scattering solutions for nonspherical particles with size parameters between 10 and 30 are lacking. Extensive research is required.

Implications of the scattering and absorption properties of nonspherical particles are discussed with respect to remote sensing and clouds and climate. We show that determination of the optical depth and height of cirrus clouds using visible and IR channels must use appropriate phase functions for ice crystals. Use of an equivalent sphere model would lead to a significant overestimate and underestimate of the cloud optical depth and height, respectively. The horizontal orientation property of ice crystals within some cirrus clouds and the scattering characteristics of bullet rosettes could be important in the interpretation of bidirectional reflectance measurements. With respect to polarization measurements for ice clouds, interpretations can not be made by spherical models, which produce a large polarization at the rainbow angle

that does not exist for hexagonal ice crystals. Polarization data from reflected sunlight can be used to differentiate between ice and water clouds. With respect to lidar backscattering, ice crystals generate significant depolarization in the returned power, which is dependent on the shape and orientation of ice crystals. It is not possible to interpret the backscattering patterns using spherical models. Moreover, we show that hollow structure in the columns reduces significantly the backscattering energy and can be important in the interpretation of lidar returns from ice clouds.

Interpretation of broadband solar albedo for cirrus clouds must use the scattering and absorption properties of hexagonal ice crystals. The equivalent spherical assumption substantially underestimates the solar albedo values, because of stronger forward scattering and larger absorption by spherical particles. For most cirrus clouds, the net cloud radiative forcing is positive, implying that the greenhouse effect outweighs the solar albedo effect. If the radiative properties of equivalent spheres were used, the cloud radiative forcing value increases; a result produced by smaller solar albedos. Using a onedimensional cloud and climate model, temperature perturbations, generated by varying the IWP of cirrus clouds, are computed by incorporating the radiative properties of hexagonal ice crystals and spheres. The spherical model has a larger temperature increase (by about 0.4 K) than the hexagonal ice crystal model. In light of the one-dimensional results presented herein, it appears important to use the scattering and absorption properties of appropriate nonspherical ice crystal/aerosol models in radiation calculations in conjunction with climate modeling and climate sensitivity analysis.

ACKNOWLEDGEMENTS

Research contained in this paper has been supported by the National Science Foundation grant ATM90-24217, NASA grants NAG5-1050 and NAG1-1048, and the Air Force Office of Scientific Research grant AFOSR91-0039. We thank Steve Ou and Qiang Fu for providing a number of illustrations presented in the paper.

REFERENCES

Ackerman, S.A., Smith, W.L., Spinhirne, J.D. and Revercomb, H.E., 1990: The 27–28 October 1986 FIRE IFO cirrus case study: Spectral properties of cirrus clouds in the 8–12 μm window. Mon. Weather Rev., 118: 2377–2388.

Asano, S. and Sato, M., 1980. Light Scattering by randomly oriented spheroidal particles. Appl. Opt., 19: 962–974.

Asano, S. and Yamamoto, G., 1975. Light scattering by a spheroidal particle. Appl. Opt., 14: 29–49.

Barber, P. and Yeh, C., 1975. Scattering of electromagnetic waves by arbitrarily shaped dielectric bodies. Appl. Opt., 14: 2864–2872.

Cai, Q. and Liou, K.N., 1982. Polarized light scattering by hexagonal ice crystals: Theory. Appl. Oct., 21: 3569–3580.

Coffeen, D.L., 1979. Polarization and scattering characteristics in the atmosphere of Earth, Venus, and Jupiter. J. Opt. Soc. Am., 69: 1051–1064.

Coleman, R.F. and Liou, K.N., 1981. Light scattering by hexagonal ice crystals. J. Atmos. Sci., 38: 1260–1271.

Draine, B.T., 1988. The discrete-dipole approximation and its application to interstellar graphite grains. Astrophys. J., 333: 848–872.

Dugin, V.P. and Mirumyants, S.O., 1976. The light scattering matrices of artificial crystalline clouds. Izv. Acad. Sci. USSR Atmos. Ocean. Phys., 12: 988–991.

Flatau, P.J., Stephens, G.L. and Draine, B.T., 1990. Light scattering by rectangular solids in the discrete-dipole approximation: a new algorithm exploiting the Block-Toeplitz structure. J. Opt. Soc. Am. A., 4: 593–600.

Fletcher, N.H., 1962. The Physics of Rain Clouds. Cambridge University Press, Cambridge, 340 pp.

Goodman, J.J., Draine, B.T. and Flatau, P.J., 1991. Application of fast-Fourier-transform techniques to the discrete-dipole approximation. Opt. Lett., 16: 1198–1200.

Greenberg, J.M., Lind, A.C., Wang, R.T. and Libelo, L.F., 1967. Scattering by nonspherical system. In: R.L. Rowell and F.S. Stein (Editors), Electromagnetic Scattering, Gordon and Breach, New York, pp. 3–54.

Greenler, R., 1980. Rainbows, Halos, and Glories. Cambridge University Press, Cambridge, 195 pp.

Hage, J.I., Greenberg, J.M. and Wang, R.T., 1991. Scattering from arbitrarily shaped particles: theory and experiment. Appl. Opt., 30: 1141–1152.

Heymsfield, A.J. and Knollenberg, R.G., 1972. Properties of cirrus generating cells. J. Atmos. Sci., 29: 1358–1366.

Holland, A.C. and Gagne, G., 1970. The scattering of polarized light by polydisperse systems of irregular particles. Appl. Opt., 9: 1113–1121.

Iskander, M.F., Lakhtakia, A. and Durney, C., 1983. A new procedure for improving the solution stability and extending the frequency range of the EBCM. IEEE Trans. Antennas and Propagat., AP-31: 317–324.

Jacobowitz, H., 1971. A method for computing transfer of solar radiation through clouds of hexagonal ice crystals. J. Quant. Spectrosc. Radiat. Transfer, 11: 691–695.

Kerker, M., 1969. The Scattering of Light and Other Electromagnetic Radiation. Academic Press, New York, 666 pp.

Liou, K.N., 1972. Light scattering by ice clouds in the visible and infrared: a theoretical study. J. Atmos. Sci., 29: 524–536.

Liou, K.N., 1980. An Introduction to Atmospheric Radiation. Academic Press, New York, 392 pp.

Liou, K.N. and Lahore, H., 1974. Laser sensing of cloud composition: A backscatter depolarization technique. J. Appl. Meteor., 13: 257–263.

Liou, K.N. and Ou, S.C., 1989. The role of cloud microphysical processes in climate: An assessment from a one-dimensional perspective. J. Geophys. Res., 94: 8599–8607.

Lord Rayleigh, 1918. The dispersal of light by a dielectric cylinder. Phil. Mag., 36: 365–376.

Minnis, P., Young, D., Heck, P., Liou, K.N. and Takano, Y., 1992. Satellite analyses of cirrus cloud properties during the FIRE phase-II cirrus intensive field observations over Kansas. 11th Int. Conf. Clouds and Precipitation, Montreal, Canada, August 17–21, pp. 480–483.

Mugnai, A. and Wiscombe, W.J., 1986. Scattering from nonspherical Chebyshev particles. 1:

Cross sections, single-scattering albedo, asymmetry factor, and backscattered fraction. Appl. Opt,, 25: 1235–1244.
Mugnai, A. and Wiscombe, W.J., 1989. Scattering from nonspherical Chebyshev particles. 3: Variability in angular scattering patterns. Appl. Opt., 28: 3061–3073.
Muinonen, K., Lumme, K., Peltoniemi, J. and Irvine, W.M., 1989. Light scattering by randomly oriented crystals. Appl. Opt., 28: 3051–3060.
Nikiforova, N.K., Pavlova, L.N., Petrushin, A.G., Snykov, V.P. and Volkovitsky, O.A., 1977. Aerodynamic and optical properties of ice crystals. J. Aerosol Sci., 8: 243–250.
Platt, C.M.R., Abshire, N.L. and McNice, G.T., 1978. Some microphysical properties of an ice cloud from lidar observations of horizontally oriented crystals. J, Appl. Met., 17: 1220–1224.
Pollack, J.B. and Cuzzi, J.N., 1980. Scattering by nonspherical particles of size comparable to a wavelength: a new semi-empirical theory and its application to tropospheric aerosols. J. Atmos. Sci., 37: 868–881.
Purcell, E.M. and Pennypacker, C.R., 1973. Scattering and absorption of light by nonspherical dielectric grains. Astrophys. J., 186: 705–714.
Rockwitz, K.D., 1989. Scattering properties of horizontally oriented ice crystal columns in cirrus clouds. Part 1. Appl. Opt., 28: 4103–4110.
Sassen, K., 1976. Polarization diversity lidar returns from virga and precipitation: Anomalies and the bright band analogy. J. Appl. Meteorol., 15: 292–300.
Sassen, K. and Liou, K.N., 1979. Scattering of polarized laser light by water droplet, mixed phase, and ice crystal clouds: I. Angular scattering patterns. J. Atmos. Sci., 36: 838–851.
Singham, S.B. and Bohren, C.F., 1987. Light scattering by an arbitrary particle: a physical reformation of the coupled dipole method. Opt. Lett., 12: 10–12.
Stackhouse, P.W. and Stephens, G.L., 1991. A theoretical and observational study of the radiative properties of cirrus: results from FIRE 1986. J. Atmos. Sci., 48: 2044–2059.
Takano, Y. and Jayaweera, K., 1985. Scattering phase matrix for hexagonal ice crystals computed from ray optics. Appl. Opt., 24: 3254–3263.
Takano, Y. and Liou, K.N., 1989. Solar radiative transfer in cirrus clouds. Part I: Single-scattering and optical properties of hexagonal ice crystals. J. Atmos. Sci., 46: 3–19.
Takano, Y., Liou, K.N. and Minnis, P., 1992. The effects of small ice crystals on cirrus infrared radiative properties. J. Atmos. Sci., 49: 1487–1493.
van de Hulst, H.C., 1957. Light Scattering by Small Particles. Wiley, New York, 470 pp.
Volkovitsky, O.A., Pavlova, L.N. and Petrushin, A.G., 1980. Scattering of light by ice crystals. Izv. Acad. Sci. USSR. Atmos. Ocean. Phys., 198: 90–102.
Wait, J.R., 1955. Scattering of a plane wave from a circular dielectric cylinder at oblique incidence. Can. J. Phys., 33: 189–195.
Waterman, P.C., 1965. Matrix formulation of electromagnetic scattering. Proc. IEEE, 53: 805–812.
Wendling, P., Wendling, R. and Weickmann, H.K., 1979. Scattering of solar radiation by hexagonal ice crystals. Appl. Opt., 18: 2663–2671.
Wiscombe, W.J. and Mugnai, A., 1988. Scattering from nonspherical Chebyshev particles. 2: Means of angular scattering patterns. Appl. Opt., 27: 2405–2421.
Zerull, R.H., 1976. Scattering measurements of dielectic and absorbing nonspherical particles. Beitr. Phys. Atmos., 49: 168–188.
Zerull, R.H. and Giese, R.H., 1974. Microwave analogue studies. In: T. Gehrels (Editor), Planets, Stars, and Nebulae Studied with Photopolarimetry, University of Arizona Press, 901–914.
Zerull, R.H., Giese, R.H. and Weiss, K., 1977. Scattering measurements of irregular particles vs. Mie theory. Opt. Polar., 112: 191–199.